

Refractive index change measurement by quantitative microscopy phase imaging for femtosecond laser written structures

Alain Abou Khalil, Wendwesen Gebremichael, Yannick Petit, Lionel Canioni *

Université de Bordeaux, CNRS, CEA, CELIA, UMR 5107, F-33405 Talence, France

ARTICLE INFO

Keywords:

Quantitative phase imaging
Refractive index change
Femtosecond laser writing

ABSTRACT

Quantitative phase imaging has been widely exploited and developed during the last decade. This technique is efficient, allowing for quantitative and qualitative spatially resolved measurements of the refractive index profiles. However, there are some measurement limitations for thick samples when exceeding the depth of field-of-view of the imaging system. In this paper, we present an approach based on the complete Rayleigh–Sommerfeld diffraction theory, which allows quantitative retrieve of the refractive index change from the measured optical path difference, especially in the case of thick samples. This approach is validated by a comparison with experimental measurements of refractive index changes of distinct series of cylindrically shaped volume modifications inscribed by femtosecond laser irradiation in silica glass. The results presented hereby, enable quantitative measurement of refractive index change for thick embedded 3D structures.

1. Introduction

Recent developments in femtosecond laser writing (fs-LW) give rise to a realization of a rich variety of integrated photonic devices, involving both high-precision surface micromachining and 3D structuring. Definitively, a complete characterization of the photo-induced modifications is of major importance to achieve precise specifications of photonic devices. Among the characterization, the measurement of the correct refractive index change is a crucial aspect in optimizing created photonic circuits.

Nowadays, many methods are used to measure the refractive index contrast (Δn) for optical waveguides/fibers, such as the refracted near-field (RNF) [1–3] numerical aperture (NA) measurement [4–6] and quantitative phase imaging (QPI) [7,8]. The RNF technique has been widely used specially to measure the refractive index profile of fiber optics. However, one of its drawbacks and limitation is the necessity to have the object of interest at the surface of measurement. Therefore, the measurement of Δn for embedded structures inside the glass is not possible. The NA technique requires the measurements of the divergence of the guided mode in the near and far-field at different distances in order to retrieve the Δn value [9]. Yet, this method does not provide a lateral Δn profile distribution for complex guiding structures exhibiting for instance positive and negative Δn simultaneously [10,11]. More recently, many QPI techniques have been developed. The most used non-interferometric technique is the Transport of Intensity Equation (TIE) [7,12–14]. It is based on acquiring several intensity images of the focused and defocused object of interest

in order to retrieve the phase value and profile [12] which is sometimes time consuming. Other interferometric QPI techniques are widely used for phase imaging in biology [15] such as the digital holographic microscopy (DHM) [16,17] and the quasi-wave lateral shearing interferometry (QWLSI) [18]. Those latter are also used for quantitative Δn measurement of optical waveguides and fibers [8,19,20] and real-time refractive index measurements [21,22] knowing that they provide fast and robust measurements.

One of the problems using QPI for refractive index measurement could be the thickness of the object, which is often much greater than the depth of field of the microscope objective used to visualize the structures. The interferometric QPI methods mentioned hereby, cannot give a direct quantitative measurement when the sample is thick [13]. It is often necessary to section it or thin it into tiny slices (few of microns) in order to make a quantitative measurement, which is not always feasible like in the case of glasses for example.

This article addresses issues related to the calculation of the refractive index from the phase measurement or the Optical Path Difference (OPD) measurements given by commercial QPI devices. Generally, the refractive index is calculated as to be linearly proportional to the measured OPD. The main issue concerns the limits of validity of this relationship assumption: up to which object thickness the linear relationship is valid and allows to extract simply a valid refractive index value? Is it possible from an OPD measurement of thick sample to extract the correct refractive index? Hereby, we propose a complete propagation model based on Rayleigh–Sommerfeld diffraction theory enabling to extrapolate from the measured OPD a correct refractive

* Corresponding author.

E-mail address: lionel.canioni@u-bordeaux.fr (L. Canioni).

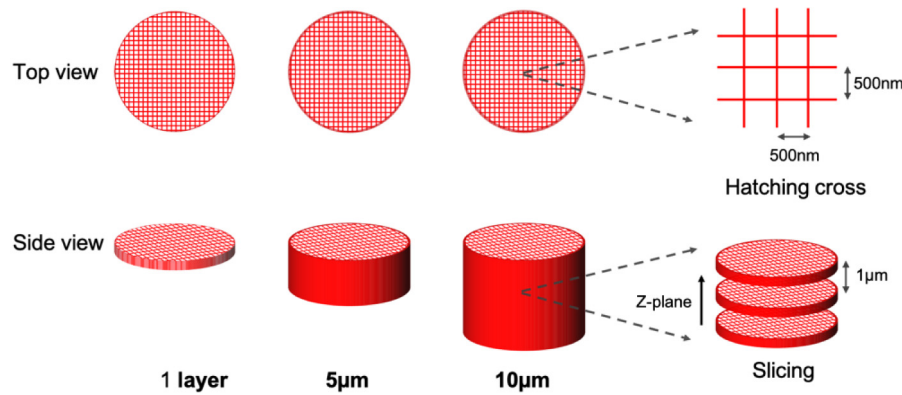


Fig. 1. Schematic presentation of the writing process of the cylinders using femtosecond laser writing technique in the F-300 silica sample.

index beyond this limit. We also highlight the limits of the standard model, based on the assumption of linear relationship between OPD, the refractive index contrast and the error of interpretation it may induce.

2. Experimental methods

2.1. Sample preparation

A commercial F-300 silica bulk glass was used to perform femtosecond laser writing of the structures. The glass sample sides were polished to optical quality allowing the laser writing and phase imaging processes. It was irradiated using a prototype femtosecond fiber laser emitting at 1030 nm wavelength, operating at 9.25 MHz repetition rate with a pulse duration of 400 fs, and an average output power of 5 W. The F-300 silica glass sample was placed on a 3D high-precision stage from Newport with a nanometric resolution of less than 15 nm. It was then irradiated using pulse energies of 130 nJ and a translation speed of 50 $\mu\text{m/s}$. The microscope objective used was a 40x - 0.75 NA Zeiss. Laser inscriptions were performed 150 μm below the surface in order to minimize the spherical aberrations and allow for the ideal imaging using a 100x-oil immersion objective. Details concerning the writing setup can be found in reference [23].

To investigate the OPD dependence on the structures' dimensions, cylinders of constant Δn (same laser parameters) with different diameters as well as different thicknesses were inscribed by laser irradiation. First, a circle is written, and then hatched with a bi-directional crossing with a step of 500 nm (Fig. 1) to ensure a spatial overlap of the laser beam, which aims at providing a smooth and uniform refractive index change all over the written disk. Then, the same writings were repeated in different planes with an inter-distance of 1 μm between each layer to ensure the overlapping in the z plane as well while forming a cylindrical shape (Fig. 1). One should note that the writings were performed from bottom to top. The diameters of the written circles presented in this section were 2 and 8 μm while the depths varied from 1 layer up to 35 μm . When writing small structures such as 2 μm disks, some uncertainty on the dimensions could be present knowing that the laser beam waist which is around ~ 1 μm .

2.2. Phase measurement method

Generally, a quantitative Δn measurement requires a highly sensitive wavefront sensor to reconstruct the distribution of the index profile. QWLSI requires only one measurement, without any moving parts, to recover phase and intensity, unlike TIE method. QWLSI allows for sampling both intensity and phase images with a higher lateral resolution than that given by the Shack-Hartmann sensor [18], for instance. In addition, it is an achromatic interferometric technique

compatible with white-light illumination of conventional wide-field microscopes.

In this work, phase images were acquired using a QWLSI sensor, SID4Bio-HR from Phasics (due to the availability of this product in our lab). QWLSI is part of shearing interferometry that consists of duplicating a field in two, displacing them laterally and then analyzing the resulting interference on a screen. This technique makes it possible to measure the phase without using a reference field [24]. After propagation, the mutual interference pattern is recorded by a CCD camera. The phase gradients from the shearing beams are recovered from the fringe deformation by means of Fourier deconvolution around the frequency of the interferogram fringe. However, at this stage, a certain gradient information is missing to recover a complete two-dimensional phase field. The space wave vector domain is six-dimensional, which implies analyzing each of the spatial interference of at least two duplicated fields with the field to be studied, these two duplicated fields being spatially shifted in orthogonal directions. The incident wavefront is indeed reproduced as two identical but inclined wavefronts. Multi-wave interferometry [18] extends this principle to more than one gradient direction. In the case of QWLSI, four replicas are created by a specific 2D diffraction grating. Gradients along two perpendicular directions are measured and integrated to determine the field intensity and phase [25,26]. Under plane wave illumination, the QWLSI allows the recovery of both the electromagnetic field intensity and its OPD gradients along two orthogonal x and y directions of the image plane. The final output of the wave front sensor is an intensity image and a phase image obtained by integration of the gradients showing the OPD of the light after passing through the sample. We consider that the OPD extracted by integration by the QWLSI sensor software is conform to reality, i.e., the phase object must have the following properties: smooth with no singularity.

When illuminating the sample with a high numerical-aperture condenser, all the waves related to different illumination angles, that do not follow the same optical path in the sample, are acquired on the same pixel [27]. Thus, the OPD cannot be quantitatively retrieved. In order to limit these mixing in the observation plane, the illumination must be spatially coherent in order to perform an accurate OPD measurement, by reducing to the minimum value the aperture of the illumination line. In our microscope, equipped with a Kohler illumination system, $NA_{\text{illumination}} \approx 0.1$ enables high contrast for phase imaging measurements while ensuring sufficient spatial coherence. For thick samples, the phase image is blurred due to of out-of-focus planes contribution. This effect reduces the spatial resolution but also downgrades the OPD measurement. [15] This is a main issue that we address in this paper for photo induced Δn measurement.

The QWLSI sensor could be installed on any microscope operating in transmission mode. In our case, it was plugged to an Axiovert 200M Zeiss Microscope, and a 100x - 1.3NA Zeiss oil objective was used to visualize the structures with a 1x tube lens. The sensor is based

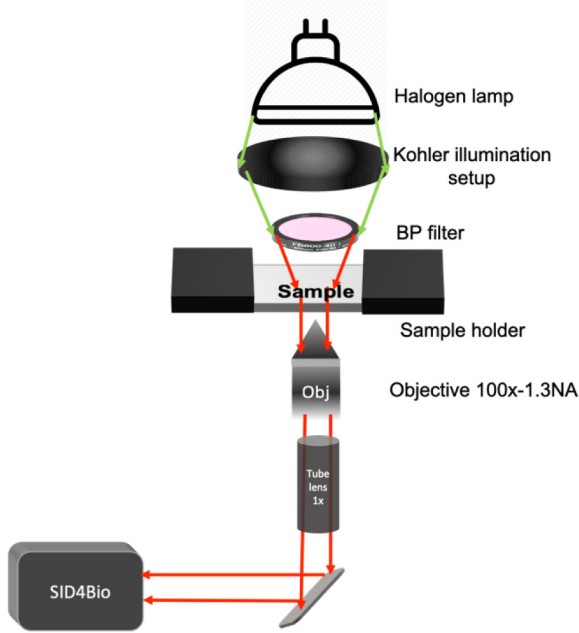


Fig. 2. Schematic presentation of the imaging setup. The QWLSI sensor (SID4Bio) is plugged to an inverted microscope operating in transmission mode.

on 300×400 phase sampling matrix, leading to a spatial sampling $s_{\text{sensor}} = 29.6 \mu\text{m}$ at the physical sensor plane. With the involved magnification $\gamma = 100\times$, the spatial sampling at the optically conjugated plane is thus $s_{\text{object}} = s_{\text{sensor}}/\gamma = 0.296 \mu\text{m}$. The depth of field is the axial distance between the nearest and farthest parts of the object that are in acceptably sharp focus in the image of this object. With our objective, and our sensor, the total Depth of Field is estimated to be less than 600 nm . A band-pass (BP) filter [600 nm–40 nm] from Thorlabs is installed after the illumination setup to reduce the chromatic aberrations effects. Knowing that the microscope used is an inverted one and that the working distance of the objective is $\sim 200 \mu\text{m}$, the sample is flipped and glued on the sample holder to ensure direct contact with the oil objective, as shown in Fig. 2.

The phase and intensity lateral measurements with a sampling rate s have to be compared with the lateral resolution of a diffraction limited microscope Re . According to the Rayleigh criterion, the lateral resolution is:

$$Re = \frac{0.61\lambda}{NA} \quad (1)$$

where λ is the source wavelength, NA the objective's numerical aperture. The lateral resolution in our setup is $Re = 0.281 \mu\text{m}$ ($\lambda = 600 \text{ nm}$ and $NA = 1.3$). In our case, the comparison of the lateral microscope resolution Re with the intensity lateral sampling $s_{\text{object}} = 0.296 \mu\text{m}$ of the SID4Bio-HR shows that the intensity sampling is almost diffraction-limited [15].

3. Theoretical model

Previous theoretical approaches for quantitative phase imaging have included both the use of linear models and direct numerical approaches. The methods of the first group are based on Born and Rytov [28–32] and on product-of-convolution (POC) approaches [33]. These models are physically well understood and simple to implement. They include several approximations concerning the object related phase shift and lead to several Taylor series or product decomposition. All of them deal with the point spread function (PSF) convolution for image formation at the conjugated image plane (namely, at the sensor position) from the object plane. Since they all rely on coherent

transmission of optical systems, the PSF is based on Fresnel–Kirchhoff diffraction. The different approximations on the amplitude and phase of contributions of out-of-field objects prevent thus any quantitative phase measurement for thick objects. These models can deliver easily quantitative OPD when the imaged object can be considered as optically thin.

More complex algorithms have been proposed to handle the case of thick objects notably the ray tracing approach [34] and direct solutions to Maxwell's equations [35]. These methods generally require extensive numerical calculation to simulate the required volume at an adequate resolution.

Our model is not computationally more intensive than those based on the first Born's approximations. It treats the object volume as a stack of thin parallel planes or slices normal to the optical axis as shown in Fig. 3. As indicated, we model transparent objects in 3D as a stack of parallel transparent slices. Each slice at position z is defined as a function of its refractive index $n(x, y, z)$ and thickness ϵ (Fig. 3).

The refractive index in the object is expressed in the form $n(x, y, z) \sim n_0 + \delta n(x, y, z)$ where $\delta n(x, y, z)$, is the difference between the refractive index of the object and the immersion medium n_0 . The optical behavior of each object slice is modeled by an exponential complex phase function $f(x, y, z) = \exp(ik_0 \delta n(x, y, z)\epsilon)$, where $k_0 = 2\pi/\lambda$ is the free space wave vector for wavelength λ . In the case of phase objects obtained by fs LW, absorption and backscatter are neglected. For simplicity and comparison, a linear phase model that neglects diffraction and provides an optical path difference named OPD_l , is given by:

$$OPD_l(x, y) = \int_0^{Z_{\text{obj}}} \delta n(x, y, z) dz \quad (2)$$

OPD_l is calculated over Z_{obj} , the total physical thickness of the object along the optical axis, and Z_{obj} can be measured experimentally. In cases where the refractive index change is a homogeneous one, therefore OPD_l could be expressed as the following:

$$OPD_l = \Delta n \cdot Z_{\text{obj}} \quad (3)$$

Consequently, Δn_l can be expressed as:

$$\Delta n_l = OPD_l / Z_{\text{obj}} \quad (4)$$

This model will be used as a basis for simple linear Δn_l measurement.

Our model uses a simple optical system approach, as shown in Fig. 3, and consists of a 3D object with known morphology and a light source. The light source is modeled as a coherent plane wave. The imaging model is as follows: light propagates along the optical axis and interacts with the object i.e. the different slices. Propagation to the imaging plane is accounted for our model using complete Rayleigh–Sommerfeld's diffraction theory [36]. As in Born's first approximation, we compute the total electric field as a superposition of the fields of all slices, assuming there is no interaction between them [37]. It models the total electric field at the given plane z , as the sum of an unperturbed incident field $E_0(x, y, z)$ that is the field propagating in a homogeneous medium, and a perturbed field $E_p(x, y, z)$ produced by the heterogeneities in the medium,

$$E(x, y, z) = E_0(x, y, z) + E_p(x, y, z) \quad (5)$$

where E is the total electric field incident at a given plane. In our case, we are analyzing thick objects. Our model assumes that each field from each slice of the object can be expressed by the pre-mentioned exponential complex function $f(x, y, z)$. It is assumed that there is no change in the amplitude distribution for each object slice after a propagation of ϵ . Thus, the expression for the field that has propagated through an object slice with thickness ϵ and location z is:

$$E(x, y, z + \epsilon) = (E_0(x, y, z) + E_p(x, y, z)) e^{(ik_0 n(x, y, z)\epsilon)} \quad (6)$$

Born's first approximation assumes an optically thin object. Thus, the perturbed field is weak compared to the incident field and its interaction with the previous object slices can be neglected [37]. Therefore,

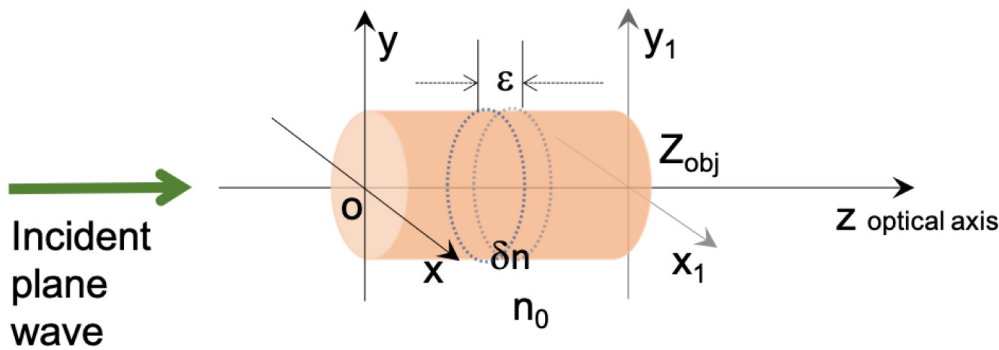


Fig. 3. Schematic presentation of the proposed model. The object of length Z_{obj} is sliced along the optical axis. Light propagates perpendicularly through each slice. For illustration, a section of an interior slice, each of thickness ϵ is shown.

the total field at $z + \epsilon$ can be expressed in terms of the interaction of the unperturbed incident field with the object slice function:

$$E(x, y, z + \epsilon) = E_0(x, y, z) e^{(ik_0 n(x, y, z) \epsilon)} \quad (7)$$

The exponential object function can be expanded with a first-order Taylor series approximation with respect to $\delta n \epsilon$ giving the following result:

$$E(x, y, z + \epsilon) = E_0(x, y, z + \epsilon)(1 + ik_0 \delta n \epsilon) \quad (8)$$

where the perturbed field from the single slice between z and $z + \epsilon$, δE_p^0 is defined as:

$$\delta E_p^0(x, y, z) = E_0 e^{ikz} (ik_0 \delta n \epsilon), \text{ if } (x, y) \in \text{Object slice} \quad (9)$$

$$\delta E_p^0(x, y, z) = 0, \text{ if } (x, y) \notin \text{Object slice}$$

where the wave vector is $k = k_0 n_0 = 2\pi n_0 / \lambda$.

To simplify the analysis and to match usual experimental conditions, the refractive index change could be considered homogeneous, therefore one can consider $\delta n(x, y, z) = \Delta n$, where Δn is the refractive index contrast between the background and the whole object. In accordance with experimental form studied, the sliced perturbed field is assumed to be a disk of diameter a and the phase object is the assembly of disks staked as a cylinder of length Z_{obj} exhibiting homogeneous refractive index change.

The perturbed field from the complete object at the image plane $E_p(x_1, y_1, Z_{\text{obj}})$ is the coherent sum of the perturbed fields of all slices through the object that have propagated to the image plane. To determine the propagation of all slices that contributed to the image plane, the near-field diffraction of the nearest slices to the image plane as well as the far-field diffraction of the farther slices must be taken into account. The only theory that can handle the different diffraction regimes without any approximation is the complete Rayleigh–Sommerfeld theory, which intrinsically includes both the Fresnel and Fresnel–Kirchhoff diffractions.

Thus, the expression for the perturbed field from a given slice at the image plane is

$$\delta E_p(x_1, y_1, z) = -i \frac{k(Z_{\text{obj}} - z)}{2\pi} \int_{\text{slice}} \text{Kernel}(x, y, x_1, y_1, z) \delta E_p^0(x, y, z) dx dy \quad (10)$$

with

$$\text{Kernel}(x, y, x_1, y_1, z) = \frac{e^{ikR_{\text{obj}}(z)}}{R_{\text{obj}}(z)^2} (1 + ikR_{\text{obj}}(z)) \quad (11)$$

This Kernel of propagation is the exact one of the Rayleigh–Sommerfeld, with $R_{\text{obj}}(z)$ the distance from a slice at position z to the image plane given by:

$$R_{\text{obj}}(z) = \sqrt{(x_1 - x)^2 + (y_1 - y)^2 + (Z_{\text{obj}} - z)^2} \quad (12)$$

The coherent sum gives the perturbed field as:

$$E_p(x_1, y_1) = \int_0^{Z_{\text{obj}} - \epsilon} \delta E_p(x_1, y_1, z) dz \quad (13)$$

Finally, we measure the phase of the field E , as the sum of the perturbed and unperturbed fields. The phase image signal can thus be expressed as:

$$\text{Signal}(x_1, y_1) = \text{Arg} \left(\frac{E_p(x_1, y_1)}{E_0 e^{ikZ_{\text{obj}}}} + 1 \right) \quad (14)$$

One can compute from $\text{Signal}(x_1, y_1)$ the OPD simulated noted as OPD_S and given by:

$$\text{OPD}_S(x_1, y_1) = \text{Signal}(x_1, y_1) \frac{\lambda}{2\pi} = Z_{\text{equ}}(a, Z_{\text{obj}}, \lambda) \Delta n(x_1, y_1) \quad (15)$$

Where $Z_{\text{equ}}(a, Z_{\text{obj}}, \lambda)$ is a correctional function obtained from our model: an equivalent interaction length.

While the simulated Δn , named Δn_s is given by:

$$\Delta n_s = \text{OPD} / Z_{\text{equ}}(a, Z_{\text{obj}}, \lambda) \quad (16)$$

Moreover, when measuring spatially tiny objects within the diffraction limit of the microscope, it is mandatory to consider the PSF convolution algorithm to take into account the spatial frequency optically filtered by the imaging system. This is not implemented in this analysis because we are dealing with objects easily resolved by our 100 x, 1.3 NA objective microscope. As for the minimum and maximum object thickness limits of this model we assume a minimum thickness of λ and a maximum of a Z_2 value detailed in the next section.

3.1. OPD simulation for thick sample

We first study the spatial profile distribution of the simulated OPDs using our model for different object thicknesses going from 1 to 8 μm for a cylinder exhibiting a constant diameter of $a = 2 \mu\text{m}$, with a given index modification of $\Delta n = 1.5 \cdot 10^{-3}$ (Fig. 4.a.). Two observations are highlighted: First, we notice that the shape of the object is blurred on the OPDs calculation as the thickness increases (Fig. 4.a.). Secondly, that the maximum OPDs seems to saturate as the thickness increases, as shown in Fig. 4.b. This is explained by the following: (a) the perturbed fields from slices far from the image plane diffract which widens the associated δE_p at the imaging plane (b) the relative phases of the far and near-fields change and the constructive interference of all δE_p does not hold any more.

In order to describe better the saturation phenomenon, the OPDs value at the center of a disk, ($x_1 = 0, y_1 = 0$, shown in Fig. 3) was simulated for different diameters and thicknesses (Z_{obj}) ranging from 1 to 10 μm and 1 to 200 μm simultaneously as presented in Fig. 5. We observe clearly and once more the saturation behavior for the OPDs when the object becomes too thick ($Z_{\text{obj}} \gg a^2 / \lambda$). When the diameter of the object is small, this saturation occurs faster (Fig. 5) which is in

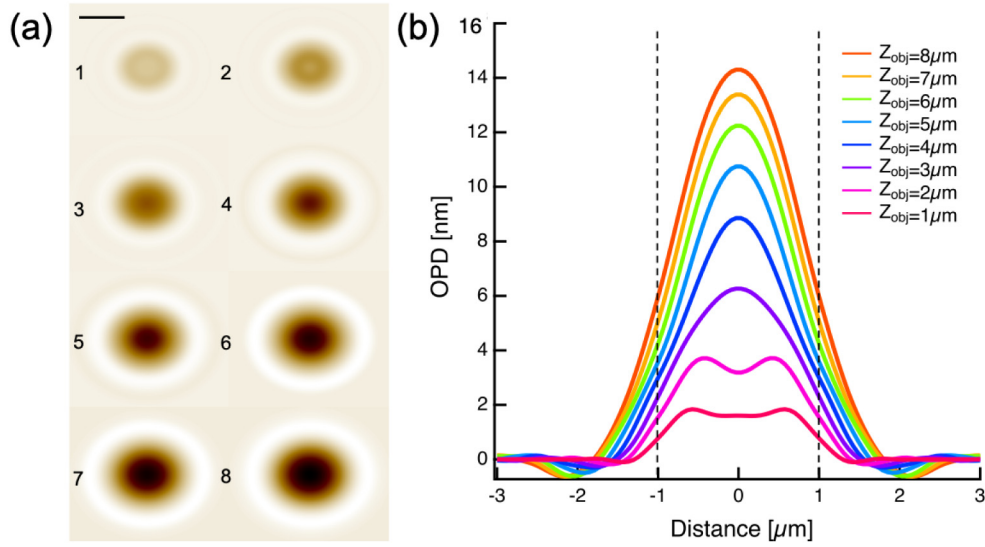


Fig. 4. (a) Calculated 2D phase image (OPDs) for cylinders of 2 μm diameter exhibiting thicknesses from 1 layer to 8 μm and index modification $\Delta n = 1.5 \cdot 10^{-3}$ (b) OPD profile extracted from Fig. 4.a for each cylinder. The scale bar corresponds to 1 μm while the numbering (1 \rightarrow 8) corresponds to the thickness of each cylinder.

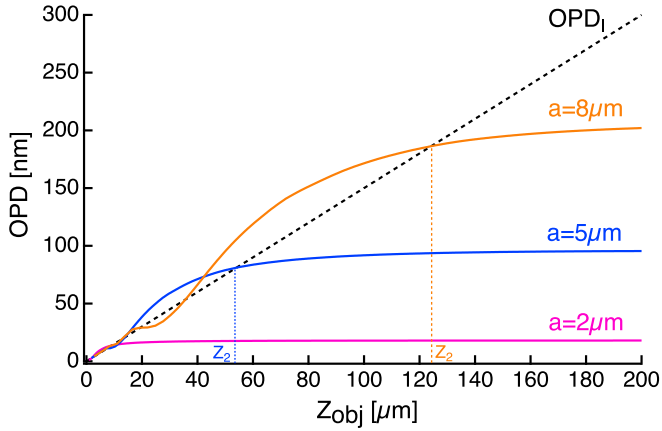


Fig. 5. Theoretical model showing the OPDs behavior for cylinders with $\Delta n = 1.5 \times 10^{-3}$, for diameters of 2, 5 and 8 μm as a function of the cylinder's thicknesses (up to 200 μm). Dashed line represents the OPD_l .

accordance with the diffraction theory (a small object diffracts more). For instance, the saturation of the OPD of a cylinder exhibiting a diameter of 2 μm occurs at around $Z_{\text{obj}} \sim 8 \mu\text{m}$ compared to $\sim 130 \mu\text{m}$ for a diameter of 8 μm when performing the measurement at $\lambda = 600 \text{ nm}$.

This behavior follows a scale law with the diameter of the diffracted object. The abscissa of the intersection of the OPDs curve with the basic model OPD_l just before saturation occurs at Z_2 (Fig. 5). This abscissa seems to be roughly around $a^2/\lambda \approx Z_2$. Before this saturation occurs, we notice that OPDs oscillates in a damped way around the linear estimation given by OPD_l (dashed line in Fig. 5). This means that, depending on the object thickness, the OPD can be higher or lower than OPD_l . This is no surprising and reflects the near-field diffraction and Talbot effects that strengthen or weaken the diffracted field at the center. For very small thicknesses (namely for thicknesses below 5 μm), the difference between OPDs and OPD_l becomes very small. This shows that our model is asymptotically equivalent to OPD_l for small object thicknesses. However, as the object thickness (Z_{obj}) increases, the number of oscillations and their period depends on the diameter of the object. These oscillations result in an OPDs values that shift away from OPD_l , therefore giving a different value of the Δn .

Each curve in Fig. 5 represents a whole simulation process for a specific cylinder diameter while varying the object thickness. It does

not seem obvious to determine from these curves a general explicit analytical law. However, when displaying OPDs normalized to OPD_l , as a function of $Z_{\text{obj}}/(5^2/\lambda)$, thus considering the 5 μm diameter object as the reference, it is interesting to notice that all the normalized curves exhibit very similar behaviors, as illustrated in Fig. 6. This curve allows for instance to define the value Z_1 which corresponds to the maximum mismatch in between the values of OPDs and OPD_l . The corresponding value on the ordinate axis is referred as the coefficient C that must be taken into account to estimate how the OPDs value is mis-estimated compared to the OPD_l . The red curve shown in Fig. 6 referred to as “functional” is obtained by averaging all the normalized OPDs for cylinder's diameters going from 2 to 10 μm . Using the functional showing in Fig. 6, one can estimate that $C \sim 1.33$ at $Z_{\text{obj}} = Z_1$. Moreover, it allows for a direct measurement of Δn . This is presented in Dataset1 in the supplemental section which provides a simple code to extract the Δn from a measured OPD value, the sample thickness and its diameter. In that case, the value of Δn_s can be estimated using the following formula:

$$\Delta n_s = \frac{\text{OPD}}{Z_{\text{obj}}} * C \quad (17)$$

Where C is the coefficient introduced above.

The absolute measurement of the refractive index change using the functional can be performed only up to $\sim Z_2$ (Fig. 6) due to the saturation of the OPD and the higher deviation of the simulated curves. For thicker objects ($Z_{\text{obj}} > Z_2$), only qualitative information can be extracted from a phase measurement. Indeed, one should note that it is not easy to determine the existence and thus the associated asymptotic value of the OPD for even thicker objects. In addition, the plane wave approximation is no longer valid anymore and experimental data are blurred, which thus limits the relevance of our model for $Z_{\text{obj}} \gg Z_2$. Overall, the functional presented in Fig. 6 allows for Δn retrieval between $0 < Z_{\text{obj}} < Z_1$ with a high precision whereas for $Z_{\text{obj}} > Z_2$ the values retrieved will exhibit a high margin of error in values.

For an object of length $Z_{\text{obj}} \ll Z_1$ OPDs and OPD_l are in the same range however for $Z_{\text{obj}} = Z_1$, the calculated OPDs and OPD_l values are:

$$\text{OPD}_s(Z_{\text{obj}} = Z_1) = \frac{4}{3} \Delta n Z_1 = \frac{2}{3} \frac{a^2}{\lambda} \Delta n \quad (18)$$

And

$$\text{OPD}_{\text{linear}}(Z_{\text{obj}} = Z_1) = \Delta n Z_1 = \frac{a^2}{2\lambda} \Delta n \quad (19)$$

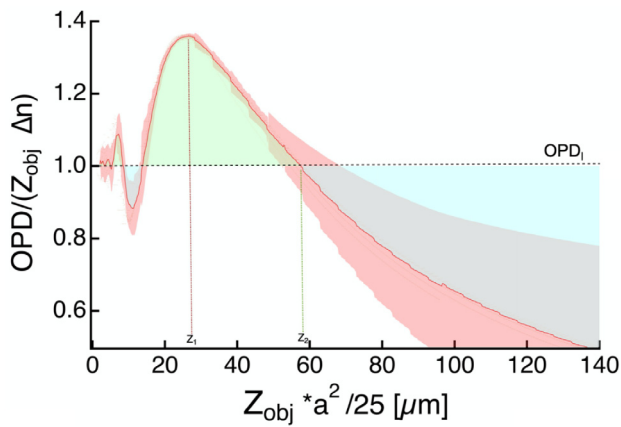


Fig. 6. Unique OPDs representation after renormalization by both the diameter and the sample thickness. Systematic comparison of the OPDs with the OPD_i over the cylinder's thickness. Red line: functional and shaded red its variance. Red dots: simulations of cylinders exhibiting diameters from 1 to 10 μm are replotted with this normalization. Green shaded and blue shaded area corresponds respectively to under and over estimation of OPD_i . Z_1 and Z_2 represent to specific points: respectively the maximum of the functional and the intersection with OPD_i . (For interpretation of the references to color in this figure legend, the reader is referred to the web version of this article.)

Therefore, the Δn could be overestimated if one uses the simple linear law of sample's optical thickness to determine it. As you can see in Figs. 5 and 6, the oscillating behavior of OPDs around OPD_i for $0 < Z_{obj} < Z_2$ can lead to an error up to +33% at $Z_{obj} = Z_1$ and down to -12% from the expected refractive index modification, if OPD_i is used instead of OPD_s for measuring the refractive index change.

4. Experimental results and discussion

In order to validate our proposed model cylinders exhibiting same Δn but different thicknesses and diameters were written using fs-LW technique in a glass sample and then imaged using a QWLSI sensor as mentioned in the methods section. Fig. 7.a shows an example of QWLSI measurement of our laser-inscribed sample showing cylinders with a diameter of 8 μm , exhibiting different thicknesses going from 1 layer (estimated numerically to $\sim 1.5 \mu\text{m}$ of effective thickness) up to 20 μm . As expected, due to far-field diffraction to the deepest slices, the thicker cylinders are getting blurry, as shown on the left of Fig. 7.a for structures with 15 and 20 μm diameter. This blurriness effect was also observed in simulation as shown in Fig. 4.a

The comparison between experimental and OPDs line profiles for cylinders of diameter 8 μm and lengths $Z_{obj} = 1, 5, 8, 10, 15, 20 \mu\text{m}$ is shown in Fig. 7.b. The refractive index change was adjusted and

fixed to 1.5×10^{-3} in the simulations to match experimental data. This value is generally expected for type I refractive index modification in fused silica with the used laser writing parameters. We conclude from Fig. 7.b a very good agreement between our experimental data and the simulated profiles and amplitudes. The slight discrepancies between the measured and calculated profiles can be explained by the fact that the PSF convolution is not taken into account in the present model. Nevertheless, the general shape of both the numerical and experimental profiles spans from cylindrical to conical as the depth increases indicating the validity of our model.

To highlight and confirm the main issue of measuring the OPD for thick samples using commercially available equipment, cylinders with the same Δn were written (same laser parameter), while exhibiting different thicknesses. Two diameters were taken into consideration 2 and 8 μm while the thickness of the cylinders varied from 1 layer to 20 μm and 1 layer to 35 μm simultaneously. Then OPD measurements were performed using QWLSI sensor as mentioned in the methods section.

• Case of 2 μm -diameter cylinders

For a 2 μm diameter cylinder, the experimental OPD tends to saturate after a value of thickness of $\sim 8 \mu\text{m}$ as shown in Fig. 8.a. For instance, the same OPD value is measured for cylinders exhibiting thicknesses from 10 to 20 μm . If we extract the Δn from those measurements using the mostly used linear model i.e. $\Delta n_i = OPD/Z_{obj}$, one can clearly see that the extracted Δn_i is going to be underestimated for thicknesses higher than 8 μm as shown in Fig. 8.b. In order to explain better, let us consider a cylinder of $\sim 5 \mu\text{m}$ thickness ($a=2 \mu\text{m}$) with a homogeneous Δn of 1.5×10^{-3} . Then we start stacking the same cylinder in the z plane to have a thickness of 20 μm . When measuring the OPD values and extracting the Δn for both, we will see a huge shift in the Δn value between them as shown in Fig. 8.b. The Δn_i value for a 5 μm thickness cylinder is $\sim 1.5 \times 10^{-3}$ while for a 20 μm cylinder it is $\sim 5 \times 10^{-4}$ which is not the good value. Stacking the same identical medium will not deviate the Δn of the medium but only increases the OPD generated by this thickness. Yet, we can see that the OPD is saturating as explained in Section 3.1 and therefore our Δn_i values are wrong for thick samples.

Using our model, one can simulate and fit all the experimental OPD values while relying on the diameter of the cylinder, the thickness, one experimental OPD value and the wavelength of measurement. The simulation shown in Fig. 8.a. is obtained by fixing the Δn_s value to 1.5×10^{-3} and adjusting slightly the diameter to 2.4 μm . Moreover, the shades on the simulation curve indicates the model tolerance by adjusting the diameter of $\pm 0.2 \mu\text{m}$ and Δn_s of $\pm 10^{-4}$ for all the presented data. Once the right Δn_s value is found which in this case is 1.5×10^{-3} , then the linear OPD_i curve is presented as shown in Fig. 8.a. This simulated curve ($OPD_{linear} = 1.5 \cdot 10^{-3} \times Z_{obj}$) indicates behavior that the OPD_i must have. The shades represented on the OPD_i curve refers to a Δn variation of $\pm 10^{-4}$.

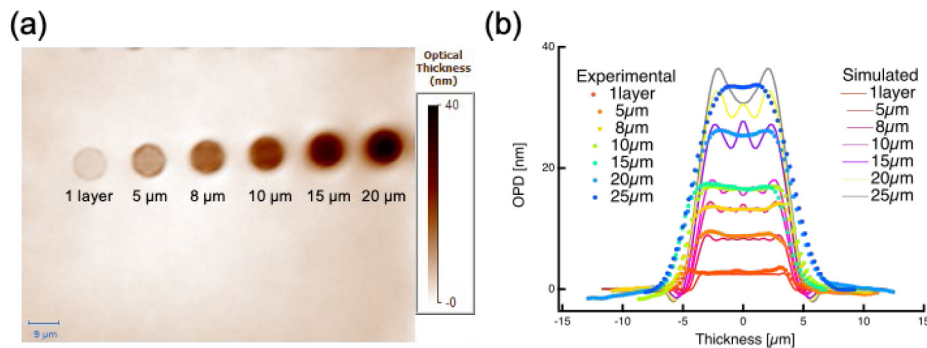


Fig. 7. (a) Phase image of the SID4Bio showing different cylinders with constant diameter exhibiting different thicknesses going from 1 layer up to 20 μm . (b) OPDs horizontal cross section of Fig. 7.a, represented by dots. Cylinder diameter is 8 μm while the thicknesses are $Z_{obj} = 1, 5, 8, 10, 15, 20$ and 25 μm for experiment data while associated simulations are represented in plain lines, $Z_{obj} = 1, 5, 8, 10, 15, 20$, and 25 μm . The refractive index change has been adjusted to the constant value of 1.5×10^{-3} in the whole simulations.

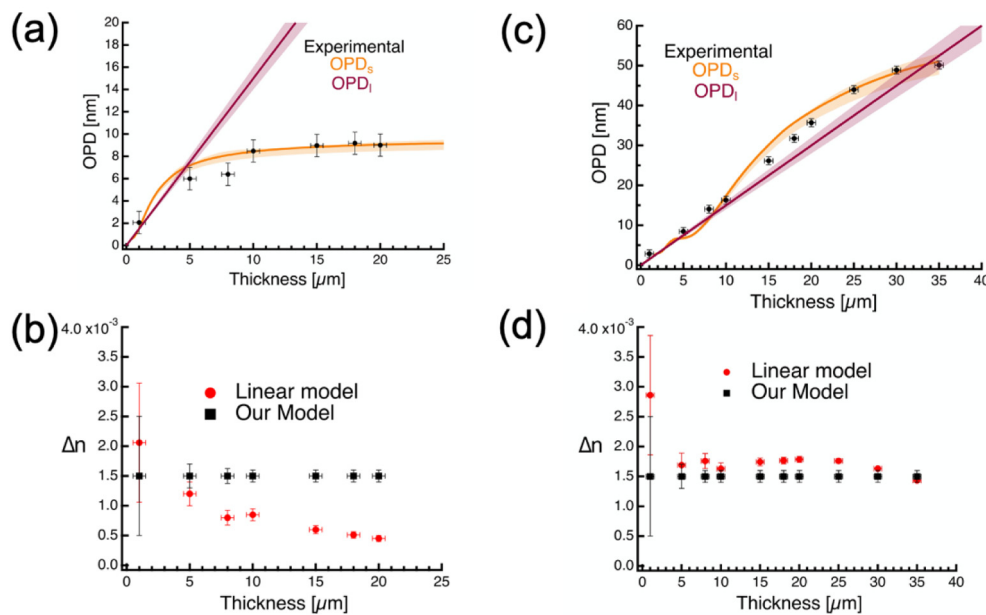


Fig. 8. OPD (dots) and OPDs (line) for a cylinder exhibiting a diameter of (a) 2 μm for different thicknesses. The simulations adjusted to a diameter of 2.4 μm and Δn of 1.5×10^{-3} , (c) 8 μm diameter for different thicknesses. OPD_l presenting the linear values of OPD for a fix Δn of 1.5×10^{-3} . The simulations were adjusted to a diameter of 7.8 μm and a Δn of 1.5×10^{-3} . The bars represent the experimental error estimated to be ± 1 nm. The shading represents the estimated simulated error by changing the diameter of ± 0.2 μm and Δn of $\pm 10^{-4}$ for all the presented data. Δn values extracted from the OPD measurements from linear model (red dots), Δn values extracted from our model (black dots) for (b) 2 μm diameter cylinder (d) 8 μm diameter cylinder. The error bars represent the error on the measurement of 1 nm for the OPD and 500 nm for the thickness.. (For interpretation of the references to color in this figure legend, the reader is referred to the web version of this article.)

• Case of 8 μm -diameter cylinders

For cylinders exhibiting a diameter of 8 μm and up to a thickness of 35 μm , the experimental OPD does not seem to saturate yet, however, it oscillates in a damped way around the real value of the Δn as shown in Fig. 8.b. The experimental results totally fit with our model presented in Fig. 5, where we show that the OPD saturation and that it is highly dependent on the diameter of the object imaged. Extracting the Δn from the measured values in this case leads to a slightly over-estimated value. In order to generalize our approach to more complex objects, here is our recommendation: for objects that are uniform by longitudinal translation (z direction) but have a more complex shape than a simple cylinder and due to the saturation of the OPD as a function of the diameter of the object, a transverse measurement completes well the above analysis and could allow for better 3D reconstruction.

5. Conclusion

In this paper, a model based on complete Rayleigh–Sommerfeld diffraction theory allowing the measurement of quantitative values of refractive index modification for thick objects exceeding the depth of view of the imaging system using QWLSI method is presented. We observed that the measured OPD of the object starts to saturate when the thickness of the object verifies $Z_{\text{obj}} > a^2/\lambda$. On the other hand, for thinner objects with $Z_{\text{obj}} < a^2/\lambda$, the OPD oscillates around the OPD_l growth with the depth of object, which can lead to a maximum over- or under-estimation of the refractive index of +33% or -12% respectively. In this range, we defined a functional that allows us to extract the index modification, simply and directly by considering the objects' dimensions. We also provide an excel sheet that exploit experimental OPD measurement and extract the Δn as a function of the thickness and diameter of the structure for cylindrical shapes. Finally, the theoretical model was validated experimentally by measuring the OPD of cylinders written using femtosecond laser writing technique in glass. We believe that this publication and the methodology explained will enable the user to quantitatively measure the refractive index change values with better accuracy. In addition, for future work, to perform a complete 3D Δn measurement on 3D phase object, different OPD measurements and analyses could be done in different planes to reconstruct the 3D Δn distribution like in 3D tomography.

Declaration of competing interest

The authors declare that they have no known competing financial interests or personal relationships that could have appeared to influence the work reported in this paper.

Acknowledgments

Authors would like to thank Bruno Bousquet for his feedbacks and Jean Philippe Bérubé and Réal Vallée for providing the fused silica sample.

Funding

This research was funded by French National Research Agency (ANR), in the framework of the “Investments for the Future” program, with the reference number LAPHIA ANR - N°ANR-10-IDEX-03-02. The project has also received funding from the European Union's Horizon 2020 research and innovation program under the Marie Skłodowska-Curie grant agreement No 823941.

Appendix A. Supplementary data

Supplementary material related to this article can be found online at <https://doi.org/10.1016/j.optcom.2020.126731>.

References

- [1] A. Neyer, Direct measurement of refractive index profiles of Ti:LiNbO₃ slab waveguides, in: H.-P.J. Nolting, R. Ulrich (Eds.), *Integrated Optics*, Springer Berlin Heidelberg, 1985, pp. 67–70.
- [2] L. McCaughan, E. Bergmann, Index distribution of optical waveguides from their mode profile, *J. Lightwave Technol.* 1 (1983) 241–244.
- [3] K. Morishita, Index profiling of three-dimensional optical waveguides by the propagation-mode near-field method, *J. Lightwave Technol.* 4 (1986) 1120–1124.
- [4] T. Calmano, A.-G. Paschke, S. Müller, C. Kränkel, G. Huber, Curved Yb:YAG waveguide lasers, fabricated by femtosecond laser inscription, *Opt. Express* 21 (2013) 25501–25508.

- [5] H. Liu, Y. Jia, J.R. Vázquez de Aldana, D. Jaque, F. Chen, Femtosecond laser inscribed cladding waveguides in Nd:YAG ceramics: Fabrication, fluorescence imaging and laser performance, *Opt. Express* 20 (2012) 18620–18629.
- [6] C. Zhang, et al., Channel waveguide lasers in Nd:GGG crystals fabricated by femtosecond laser inscription, *Opt. Express* 19 (2011) 12503–12508.
- [7] E. Bélanger, J.-P. Bérubé, B. de Dorlodot, P. Marquet, R. Vallée, Comparative study of quantitative phase imaging techniques for refractometry of optical waveguides, *Opt. Express* 26 (2018) 17498–17510.
- [8] A. Abou Khalil, et al., Direct laser writing of a new type of waveguides in silver containing glasses, *Sci. Rep.* 7 (2017) 11124.
- [9] J. Hernandez-Rueda, et al., All-optical characterization of fs-laser induced refractive index changes in bulk and at the surface of zinc phosphate glasses, in: P.R. Heisterkamp, M. Meunier, S. Nolte (Eds.), in: *Frontiers in Ultrafast Optics: Biomedical, Scientific, and Industrial Applications XV*, 9355, SPIE, 2015, pp. 152–158.
- [10] A. Abou Khalil, et al., Comparative study between the standard type I and the type A femtosecond laser induced refractive index change in silver containing glasses, *Opt. Mater. Express* 9 (2019) 2640–2651.
- [11] J.-P. Bérubé, M. Bernier, R. Vallée, Femtosecond laser-induced refractive index modifications in fluoride glass, *Opt. Mater. Express* 3 (2013) 598–611.
- [12] A. Barty, K.A. Nugent, D. Paganin, A. Roberts, Quantitative optical phase microscopy, *Opt. Lett.* 23 (1998) 817–819.
- [13] J.A. Rodrigo, T. Alieva, Rapid quantitative phase imaging for partially coherent light microscopy, *Opt. Express* 22 (2014) 13472–13483.
- [14] A. Jesacher, P.S. Salter, M.J. Booth, Refractive index profiling of direct laser written waveguides: Tomographic phase imaging, *Opt. Mater. Express* 3 (2013) 1223–1232.
- [15] P. Bon, G. Maucort, B. Wattellier, S. Monneret, Quadriwave lateral shearing interferometry for quantitative phase microscopy of living cells, *Opt. Express* 17 (2009) 13080–13094.
- [16] G. Coppola, et al., A digital holographic microscope for complete characterization of microelectromechanical systems, *Meas. Sci. Technol.* 15 (2004) 529–539.
- [17] F. Charrière, et al., Characterization of microlenses by digital holographic microscopy, *Appl. Opt.* 45 (2006) 829–835.
- [18] J. Primot, L. Sogno, Achromatic three-wave (or more) lateral shearing interferometer, *J. Opt. Soc. Amer. A* 12 (1995) 2679–2685.
- [19] J. Lapointe, et al., Nonlinear increase, invisibility, and sign inversion of a localized fs-laser-induced refractive index change in crystals and glasses, *Light. Sci. Appl.* 9 (2020) 64.
- [20] T.T. Fernandez, S. Gross, A. Arriola, K. Privat, M.J. Withford, Revisiting ultrafast laser inscribed waveguide formation in commercial alkali-free borosilicate glasses, *Opt. Express* 28 (2020) 10153–10164.
- [21] T. Balciunas, A. Melninkaitis, G. Tamosauskas, V. Sirutkaitis, Time-resolved off-axis digital holography for characterization of ultrafast phenomena in water, *Opt. Lett.* 33 (2008) 58–60.
- [22] V. Pagliarulo, A. Calabuig, S. Grilli, P. Ferraro, Direct quantitative imaging of the writing stage in a photosensitive azopolymer by digital holography, *Soft Matter* 15 (2019) 7809–7813.
- [23] E. Lee, et al., Sub-diffraction-limited fluorescent patterns by tightly focusing polarized femtosecond vortex beams in a silver-containing glass, *Opt. Express* 25 (2017) 10565–10573.
- [24] J.-C. Chanteloup, F. Druon, M. Nantel, A. Maksimchuk, G. Mourou, Single-shot wave-front measurements of high-intensity ultrashort laser pulses with a three-wave interferometer, *Opt. Lett.* 23 (1998) 621–623.
- [25] C. Wang, Q. Fu, X. Dun, W. Heidrich, Quantitative phase and intensity microscopy using snapshot white light wavefront sensing, *Sci. Rep.* 9 (2019) 13795.
- [26] P. Bon, S. Monneret, B. Wattellier, Noniterative boundary-artifact-free wavefront reconstruction from its derivatives, *Appl. Opt.* 51 (2012) 5698–5704.
- [27] J. Primot, Theoretical description of Shack–Hartmann wave-front sensor, *Opt. Commun.* 222 (2003) 81–92.
- [28] T.E. Gureyev, T.J. Davis, A. Pogany, S.C. Mayo, S.W. Wilkins, Optical phase retrieval by use of first Born- and Rytov-type approximations, *Appl. Opt.* 43 (2004) 2418–2430.
- [29] C.J.R. Sheppard, M. Gu, Modeling of 3D imaging in brightfield microscope systems, in: T.J. Schulz, D.L. Snyder (Eds.), in: *Image Reconstruction and Restoration*, 2302, SPIE, 1994, pp. 352–358.
- [30] C. Preza, D.L. Snyder, J.-A. Conchello, Theoretical development and experimental evaluation of imaging models for differential-interference-contrast microscopy, *J. Opt. Soc. Amer. A* 16 (1999) 2185–2199.
- [31] C.J. Bellair, et al., Quantitative phase amplitude microscopy IV: Imaging thick specimens, *J. Microsc.* 214 (2004) 62–69.
- [32] N. Streibl, Three-dimensional imaging by a microscope, *J. Opt. Soc. Amer. A* 2 (1985) 121–127.
- [33] H. Sierra, C.A. DiMarzio, D.H. Brooks, Modeling phase microscopy of transparent three-dimensional objects: A product-of-convolutions approach, *J. Opt. Soc. Amer. A* 26 (2009) 1268–1276.
- [34] F. Kagalawa, T. Kanade, Computational model of image formation process in DIC microscopy, in: T.T. Lu, et al. (Eds.), in: *Three-Dimensional and Multidimensional Microscopy: Image Acquisition and Processing V*, 3261, SPIE, 1998, pp. 193–204.
- [35] J.L. Hollmann, A.K. Dunn, C.A. DiMarzio, Computational microscopy in embryo imaging, *Opt. Lett.* 29 (2004) 2267–2269.
- [36] G.D. Gillen, S. Guha, Modeling and propagation of near-field diffraction patterns: A more complete approach, *Amer. J. Phys.* 72 (2004) 1195–1201.
- [37] A.C. Kak, M. Slaney, *Principles of Computerized Tomographic Imaging*, 2001, <http://dx.doi.org/10.1137/1.9780898719277>.